Self-assembled ruthenium (II) metallacycles and metallacages with imidazole-based ligands and their in vitro anticancer activity

Yibo Zhao[a,b,1], Liqian Zhang[a,1], Xu Li[a], Yanhui Shi[a,2], Ruru Ding[c], Mengting Teng[c], Peng Zhang[c,2], Changsheng Cao[a,2], and Peter J. Stang[b,2]

[a]School of Chemistry and Material Science and Jiangsu Key Laboratory of Green Synthetic Chemistry for Functional Materials, Jiangsu Normal University, Xuzhou, 221116 Jiangsu, People's Republic of China; [b]Department of Chemistry, University of Utah, Salt Lake City, UT 84112; and [c]School of Life Science, Jiangsu Normal University, Xuzhou, 221116 Jiangsu, PR China

Contributed by Peter J. Stang, January 8, 2019 (sent for review October 31, 2018; reviewed by Jean-Marie P. Lehn, Gabor A. Somorjai, and Vivian Wing-Wah Yam)

Six tetranuclear rectangular metallacycles were synthesized via the [2+2] coordination-driven self-assembly of imidazole-based ditopic donor 1,4-bis(imidazole-1-yl)benzene and 1,3-bis(imidazol-1-yl)benzene, with dinuclear half-sandwich *p*-cymene ruthenium (II) acceptors $[Ru_2(\mu\text{-}\eta^4\text{-oxalato})(\eta^6\text{-}p\text{-cymene})_2](SO_3CF_3)_2$, $[Ru_2(\mu\text{-}\eta^4\text{-2,5-dioxido-1,4-benzoquinonato})(\eta^6\text{-}p\text{-cymene})_2](SO_3CF_3)_2$ and $[Ru_2(\mu\text{-}\eta^4\text{-5,8-dioxido-1,4-naphtoquinonato})(\eta^6\text{-}p\text{-cymene})_2](SO_3CF_3)_2$, respectively. Likewise, three hexanuclear trigonal prismatic metallacages were prepared via the [2+3] self-assembly of tritopic donor of 1,3,5-tri(1*H*-imidazol-1-yl)benzene with these ruthenium(II) acceptors respectively. Self-selection of the single symmetrical and stable metallacycle and cage was observed although there is the possibility of forming different conformational isomeric products due to different binding modes of these imidazole-based donors. The self-assembled macrocycles and cage containing the 5,8-dioxido-1,4-naphtoquinonato (donq) spacer exhibited good anticancer activity on all tested cancer cell lines (HCT-116, MDA-MB-231, MCF-7, HeLa, A549, and HepG-2), and showed decreased cytotoxicities in HBE and THLE-2 normal cells. The effect of Ru and imidazole moiety of these assemblies on the anticancer activity was discussed. The study of binding ability of these donq-based Ru assemblies with ctDNA indicated that the complex 9 with 180° linear 1 ligand has the highest bonding constant K_b to ctDNA.

supramolecular chemistry | self-assembly | anticancer activity

Today platinum complexes including cisplatin, carboplatin, and oxoplatin are the most widely used and effective metal-based chemotherapeutic agents in clinical cancer treatment, and it is estimated that they have been used in at least 50% of cancer treatment regimens (1–3). However, the high neurotoxicity, hepatotoxicity, nephrotoxicity, serious side effects, drug resistance, and limited activity of these Pt-base drugs indicate the need to design and develop more selective and safer metal-based drug candidates (4–6). Ruthenium complexes, a non-platinum-based alternative represents a promising new class of anticancer drugs (7), due to their low cytotoxicity, high activity in certain tumors, and especially impressive antimetastatic properties (8–10). Ruthenium shows a rich redox chemistry, and has two main oxidation states (II and III). Many organoruthenium(II) (11–17) and coordinated Ru(III) (18–20) mononuclear complexes have been found to display promising anticancer activities. For example, a large number of piano-stool arene Ru(II) complexes with monodentate pta (1,3,5-triaza-7-phosphaadamantane) or various of chelated *N,N*-, *N,O*-, *O,O*-, *C,N*-, and *P,P*- ligands have been designed and their potent anticancer activities investigated (11, 12). In fact, Ru(III) coordination complexes, [ImH]*trans*-$[RuCl_4(DMSO\text{-}S)(Im)]$ (NAMI-A, Im = imidazole) (21), [InH][trans-$RuCl_4In_2$] (KP1019, In = indazole) (22, 23), and Na[trans-$RuCl_4In_2$] (NKP-1339) (24) have entered clinical trials, and the first Ru-base prodrugs NAMI-A has reached phase II clinical trials (21).

In addition, many discrete 2D (2D) and 3D (3D) multinuclear Ru(II)-based metallacycles and metallacages (25–28), with predesigned shape, size, internal cavities, and functionality (29–33), were constructed via the coordination-driven self-assembly; they also displayed antitumor efficacy in certain cancer cells (34–39). Compared with those mononuclear complexes, the multinuclear self-assembled supermolecules may show different solubility in both lipid and water as they normally bear more positive charges (40). Furthermore, the internal cavity of the supermolecules is able to hold certain guest molecule, so they may serve as hosts to control the release of an encapsulated drug into cancer cells (41). In addition, the large-sized and high-molecular-weight multinuclear compounds could selectively enter and remain in the targeted tumor cells rather than normal cells via the enhanced permeability and retention effect (42).

Compared with the widely used pyridyl donor ligands (43, 44), construction of self-assembled complexes using imidazolyl donor

Significance

Cancer is one of the most deadly diseases. In the treatment of cancer, the success of platinum compounds has propelled the application of transition metal complexes for therapeutic design. Ruthenium compounds have emerged as promising anticancer candidates. Self-assembly strategy allows the construction of large-sized and high-molecular-weight supermolecules that may display antitumor efficacy and selectivity due to their unique biochemical properties. Herein, we describe the construction of Ru(II) tetranuclear rectangular macrocycles and hexanuclear trigonal prisms by self-assembly. The self-assembled compounds containing the 5,8-dioxido-1,4-naphtoquinonato scaffold exhibited enhanced anticancer activity on colon, breast, cervical, lung, and liver cancer cells, and decreased cytotoxicities in HEB and THLE-2 normal cells. Two of these compounds are able to kill cancer cells more effectively and selectively than cisplatin.

Author contributions: Y.S., C.C., and P.J.S. designed research; Y.Z., L.Z., X.L., R.D., M.T., and P.Z. performed research; Y.Z., Y.S., C.C., and P.J.S. analyzed data; and Y.S., C.C., and P.J.S. wrote the paper.

Reviewers: J.-M.P.L., Université Louis Pasteur-ISIS; G.A.S., UC Berkeley; and V.W.-W.Y., The University of Hong Kong.

The authors declare no conflict of interest.

[1]Y.Z. and L.Z. contributed equally to this article.

[2]To whom correspondence may be addressed. Email: yhshi@jsnu.edu.cn, zhangpeng@jsnu.edu.cn, chshcao@jsnu.edu.cn, or stang@chem.utah.edu.

This article contains supporting information online at www.pnas.org/lookup/suppl/doi:10.1073/pnas.1818677116/-/DCSupplemental.

Published online February 14, 2019.

ligands is less developed, mainly due to the unpredictable outcome of the architecture due to the less symmetric imidazole-based ligands (45, 46). As an important five-membered aromatic heterocycle, imidazole and its derivatives are widely found in both natural and synthetic functional materials (47–53). The desirable electron-rich characteristics of the imidazole ring make its binding through diverse weak interactions with a variety of enzymes and receptors in biological systems possible (54, 55).

Herein, we present the synthesis of tetranuclear metallacycles and hexanuclear metallacages by the self-assembly of binuclear half-sandwich ruthenium(II) building units $[Ru_2(\mu\text{-}\eta^4\text{-}OO\cap OO)(\eta^6\text{-}p\text{-cymene})_2](O_3SCF_3)_2$ (OO∩OO = oxalato (oxa), 2,5-dioxido-1,4-benzoquinonato (dobq) and 5,8-dioxido-1,4-naphtoquinonato (donq)) with ditopic bis(imidazolyl) benzene having different geometry and tritopic tri(imidazolyl) benzene and investigated their cytotoxicity against human cancer and normal cell lines. Their antitumor activities and cancer cell selectivities were compared with the anticancer drugs cisplatin and doxorubicin. As investigation of such structure–activity relationships helps to determine how modifying different functional groups on the ligands affects the anticancer efficacy of the complexes. The relationship between activity and cancer selectivity with the structure of the assemblies is also discussed.

Results and Discussion

Unlike a pyridine-based ligand, the imidazole-based ligands **1–3** can adopt different conformations and bonding modes due to the lack of a C_2 symmetry axis along the *N*–N direction and the free rotation of the C–N single bonds (Fig. 1). As these imidazole-based ditopic **1** and **2** ligands could adopt anti- and syn-binding modes, the reaction of linear **1** and **2** (donor) with a 0° Ru(II) clip (acceptor) may lead to two different isomeric geometric metallacycles via the [2+2] coordination-driven self-assemblies (Fig. 2). However, only a single set of NMR peaks is observed in the ^{1}H and ^{13}C NMR spectra of **7–12**, suggesting that only the symmetrical geometric isomer is selectively formed (56). The possible reason for the exclusive formation of the symmetrical geometrical isomer may be that the binding mode of the ligand in the symmetrical form in the assemblies has the least steric hindrance.

Likewise, there are also symmetrical and nonsymmetrical binding modes with the tritopic **3** ligand, therefore, two isomeric metallacages may form via the one-pot [2+3] self-assembly with a 0° Ru clip (Fig. 3). However, only a single set of NMR peaks was observed in the ^{1}H and ^{13}C NMR spectra of **13–15**, suggesting that only the symmetrical trigonal prismatic cage, with minimal steric effect between the Ru building blocks, is selectively formed (57).

As shown in Fig. 4, when the pseudo-180° ligand **1** was treated with the 0° dinuclear *p*-cymene Ru(II) acceptors **4–6** in an equimolar ratio in CH_3OH at room temperature, respectively; the rectangular metallacycles **7–9** were obtained in 72–80% yield. The formation of complexes **7–9** is confirmed by ^{1}H and ^{13}C NMR, electrospray ionization-mass spectrometry (ESI-MS), and elemental analyses. In the ^{1}H NMR spectrum of **9** (Fig. 5, *Left*), four peaks corresponding to the ligand **1** were observed in the aromatic region (8.39–6.97 ppm) that also exhibited the expected chemical shift compared with the free ligand. The protons corresponding to the *p*-cymene moiety were found in 5.82–5.60 ppm. In the ^{13}C NMR spectrum of **9** (*SI Appendix*, Fig. S8), the signal of C = O is at 172.3 ppm, and the carbon of the $^-OSO_2CF_3$ is a quartet at 121.8 ppm. Likewise, similar proton and carbon resonances were observed for compounds **7** and **8** as well (*SI Appendix*, Figs. S1, S2, S4, and S5). The ESI-MS analysis supports the formation of [2+2] self-assembled metallacycles **7–9** by the appearance of +2 charged fragment ions for **7** at *m/z* = 917.96 $[\mathbf{7}\text{-}2CF_3SO_3^-]^{2+}$; for **8** at *m/z* = 968.95 $[\mathbf{8}\text{-}2CF_3SO_3^-]^{2+}$, and for **9** at *m/z* = 1018.93 $[\mathbf{9}\text{-}2CF_3SO_3^-]^{2+}$. The experimentally observed isotopic distributions of the peaks corresponding to these fragments were consistent with their charge state (Fig. 6, *Left,* and *SI Appendix*, Figs. S3 and S6). Elemental analyses for C, H, and N for **7–9** are consistent with the proposed structures.

When the pseudo-120° ligand **2** was used, rectangles **10–12** are obtained in good yield, and the NMR spectra and ESI-MS indicate the formation of **10–12**. Six peaks corresponding to the donor **2** and five peaks corresponding to the *p*-cymene moiety were found in the ^{1}H NMR spectrum of **10** (Fig. 5, *Middle*). In the ^{13}C NMR spectrum of **10** (*SI Appendix*, Fig. S10), the C of the oxalate is at 172.4 ppm, and the $^-OSO_2CF_3$ C-signal is a quartet centered at 121.8 ppm. Similar proton and carbon resonances were observed for assemblies **11** and **12** (*SI Appendix*, Figs. S11, S12, S14, and S15). The ESI-MS for **10** ($[\mathbf{10}\text{-}2OTf^-]^{2+}$: 917.96) shows one peak that corresponds to the intact [2+2] assembly with a +2 charge as a result of the loss of two ^-OTf counter ions (Fig. 6, *Middle*); $[\mathbf{11}\text{-}2OTf^-]^{2+}$ at *m/z* 968.10 and $[\mathbf{12}\text{-}2OTf^-]^{2+}$ at *m/z* 1018.96 were also observed for **11** and **12** (*SI Appendix*, Figs. S13 and S16). These peaks are isotopically resolved and are in good agreement with their calculated theoretical distributions. These ESI-MS results support the formation of [2+2] macrocycles **10–12**.

The metallacages **13–15** are obtained via the reaction of a tritopic planar ligand **3** with Ru(II) acceptors **4–6,** respectively, in a 2:3 ratio in good yield. The NMR spectra and ESI-MS indicate the formation of symmetrical trigonal prisms **13–15**. In the ^{1}H NMR spectrum of **15** shown in the right-hand side of Fig. 5, the imidazole protons corresponding to ligand **3** appeared in the aromatic region (8.74–6.90 ppm), shifted in the range of δ = 0.20–0.32 ppm compared with the free ligand. The protons of the donq moiety and *p*-cymene moiety were also observed in the expected region (*SI Appendix*, Fig. S24). In the ^{13}C NMR spectrum of **9**, the ^-OTf carbon is a quartet at 121.8 ppm, and the carbon of the C = O is at 172.1 ppm. Similar proton and carbon resonances are also observed for the trigonal prisms **14** and **15** (*SI Appendix*, Figs. S17, S18, S20, and S21). The ESI-MS analyses support the formation of [2+3] self-assembled prismatic cages **13** at *m/z* 1412.34 $[\mathbf{13}\text{-}2CF_3SO_3^-]^{2+}$, for **14** at *m/z* 1488.13 $[\mathbf{14}\text{-}2CF_3SO_3^-]^{2+}$, and for **15** at *m/z* 1562.28 $[\mathbf{15}\text{-}2CF_3SO_3^-]^{2+}$ (Fig. 6, *Right,* and *SI Appendix*, Figs. S19 and S22). These peaks are isotopically resolved and are in good agreement with their calculated theoretical distributions.

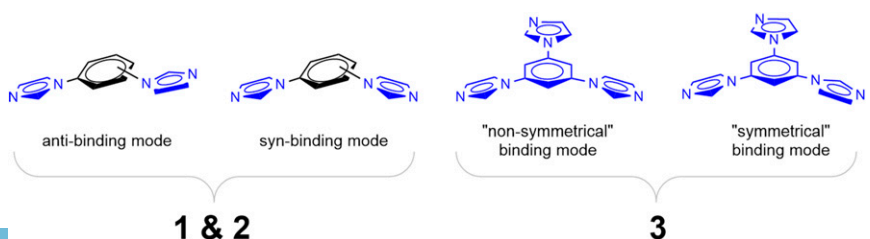

Fig. 1. Different binding modes of **1**, **2**, and **3**.

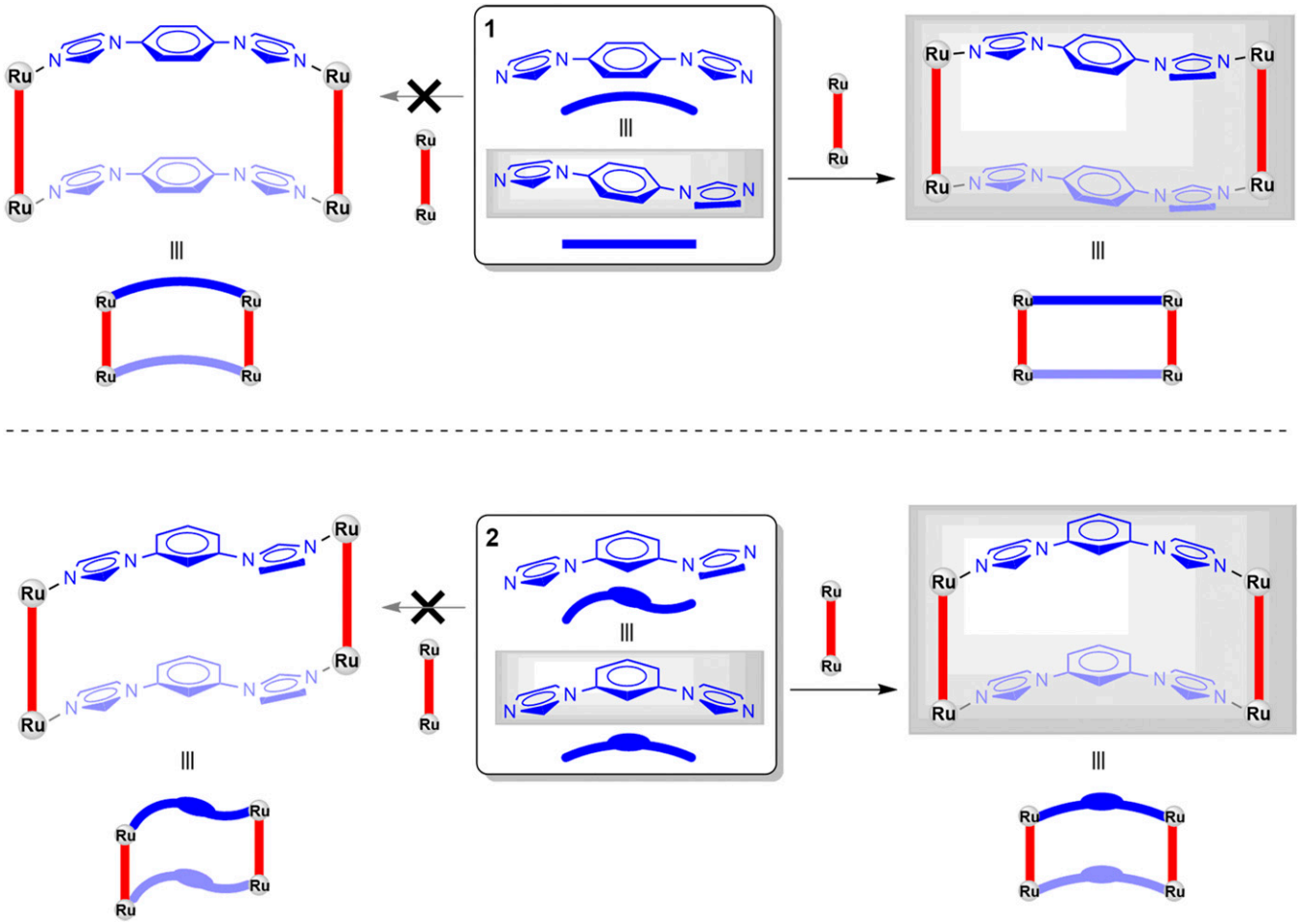

Fig. 2. Possible conformational isomeric metallacycles of a 0° Ru clip with ditopic imidazole-based ligand **1** or **2** via one-pot [2+2] self-assembly.

To gain insight into the reaction mechanism, the self-assembly of complex **15** in CD_3OD was monitored by ^1H NMR (Fig. 7). In the beginning of the reaction, besides the signals of the reactant **6** (triangles in Fig. 7) and the product **15** (squares in Fig. 7), a group of weak signals assigned to the unsymmetric geometrical isomer of **15** (circles in Fig. 7) appeared. As the reaction progressed, the peaks corresponding to **6**, the unsymmetrical isomer of **15** gradually disappeared, and only one set of signals corresponding to **15** was observed. This suggests that the reaction conditions favor the formation of the thermodynamically stable geometric isomer **15**. This is further confirmed by density functional theory (DFT) calculations.

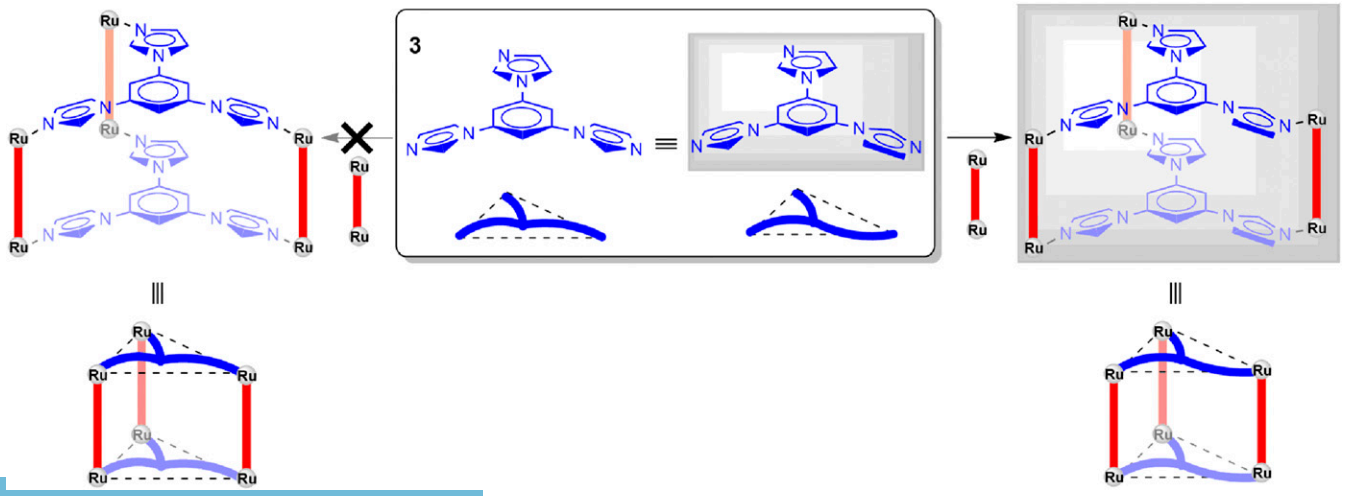

Fig. 3. Possible isomeric conformational metallacages of a 0° Ru clip with tritopic imidazole-based ligand **3** via one-pot [2+3] self-assembly.

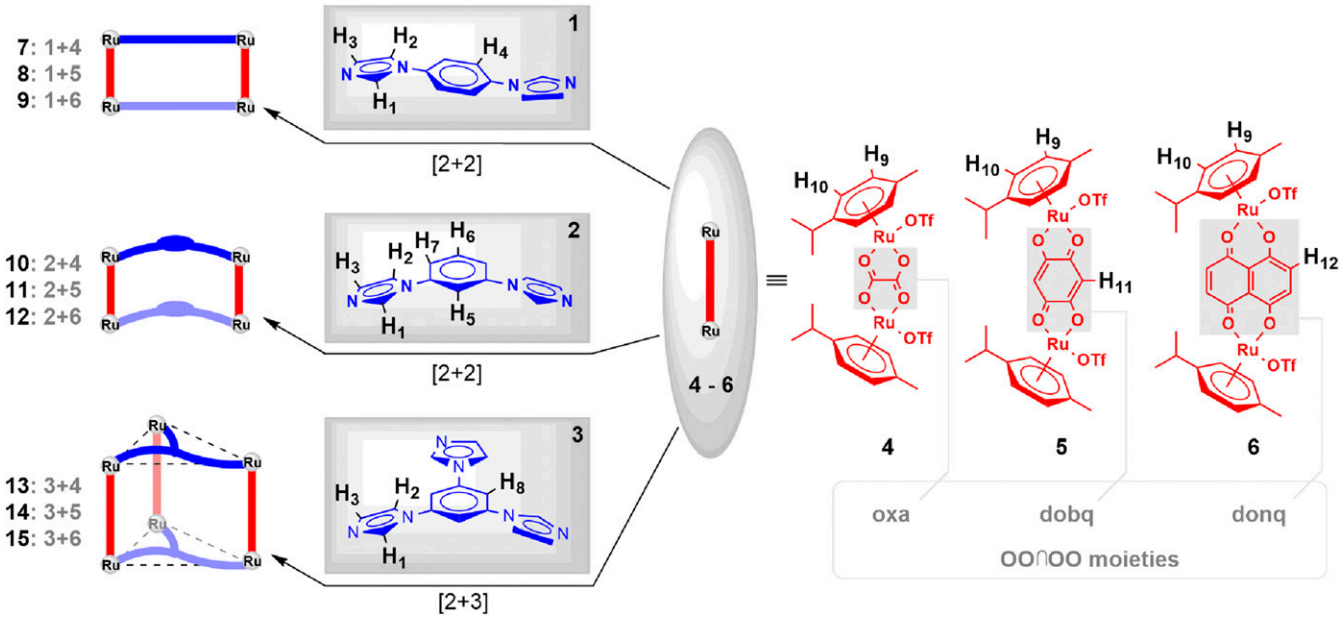

Fig. 4. Coordination-driven self-assembly of complexes **7**–**15**.

Geometry optimizations of **9**, **12**, and **15** were carried out using the B3LYP functional as implemented in Gaussian 09 (Fig. 8). The energy minimized structures of these complexes showed that imidazole ligand **1** adopts an antibonding mode for complex **9**, whereas the imidazole ligand **2** and **3** adopt a syn- and symmetrical bonding mode for complexes **12** and **15**, respectively. The optimized geometries showed that tetranuclear complex **9** has an approximate rectangular geometry and the tetranuclear **12** has complex folded rectangular geometry, while the hexanuclear metallacage **15** has a trigonal prismatic geometry. In these complexes, the two Ru centers of the Ru building unit **6** are separated by 8.39 Å, which is somewhat shorter than the distance between the two centroids of the benzene rings (8.80 Å for **9**, 9.75 Å for **12**, and 8.95 Å for **15**). The two Ru centers coordinating to the imidazole ligand are 13.85 Å (**9**), 11.26 Å (**12**), and 12.0 Å (**15**) away from each other.

These arene ruthenium assemblies are air and moisture stable in the solid state, and they can be stored in the air for more than 2 mo without any noticeable decomposition. The stability of these metallacycles and metallacages in water was investigated by ^{1}H NMR of **9**, **12**, and **15** in D_2O (*SI Appendix*, Fig. S25). No hydrolysis was observed after 24 h at room temperature, hence their stability in water will facilitate their biological applications.

To investigate the influence of different imidazole-based linkers and OO∩OO moieties (Fig. 4) on their activity, the in vitro anticancer efficacies of tetranuclear macrocycles **7**–**12** and hexanuclear prismatic cages **13**–**15** were assessed by an MTT assay in five human cancer cell lines, including HCT-116 (colon), MDA-MB-231 (breast), MCF-7 (breast), HeLa (cervical), and A549 (lung). The free imidazole (**1**–**3**) ligands and Ru-based metal clips (**4**–**6**) were tested as controls. The clinically used anticancer drug cisplatin and doxorubicin were tested as well for comparisons. These cells were exposed to various concentrations of the compounds **1**–**15**, cisplatin and doxorubicin for 48 h, and the results are summarized in Table 1. The data indicate that the assemblies containing the oxalato (**7**, **10**, and **13**) and dobq (**8**, **11**, and **14**) spacers are essentially inactive across all cell lines, whereas the donq-based scaffolds (**9**, **12**, and **15**) exhibit good anticancer activity on all tested cancer cell lines, especially compound **9**. Rectangle **9** possesses excellent anticancer activity with the lowest IC_{50} values of 0.37 μM toward HCT-116, 1.83 μM toward MDA-MB-231, and 1.14 μM toward A549 cancer cell lines, respectively, and prismatic cage **15** has the lowest IC_{50} values of 1.36 μM against MCF-7 and HeLa cancer cell lines. The three donq-based assemblies **9**, **12**, and **15** have potency comparable to doxorubicin, but better than cisplatin against all tested cancer cell lines. The IC_{50} values of all cell lines in Table 1 indicate that the free ligands **1**–**3** have no anticancer ability (>50 μM), and the arene-ruthenium acceptor **6** is less effective than compounds **9**, **12**, and **15**. These results may be rationalized by the observation that the ligands themselves are almost insoluble in the cell culture medium, hence they may only undergo

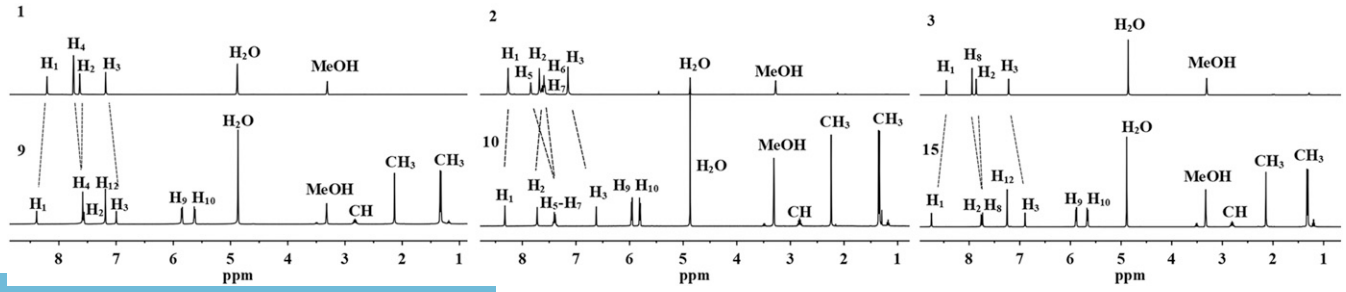

Fig. 5. The ^{1}H NMR spectra of ligand **1** and complex **9** (*Left*), ligand **2** and complex **10** (*Middle*), and ligand **3** and complex **15** (*Right*).

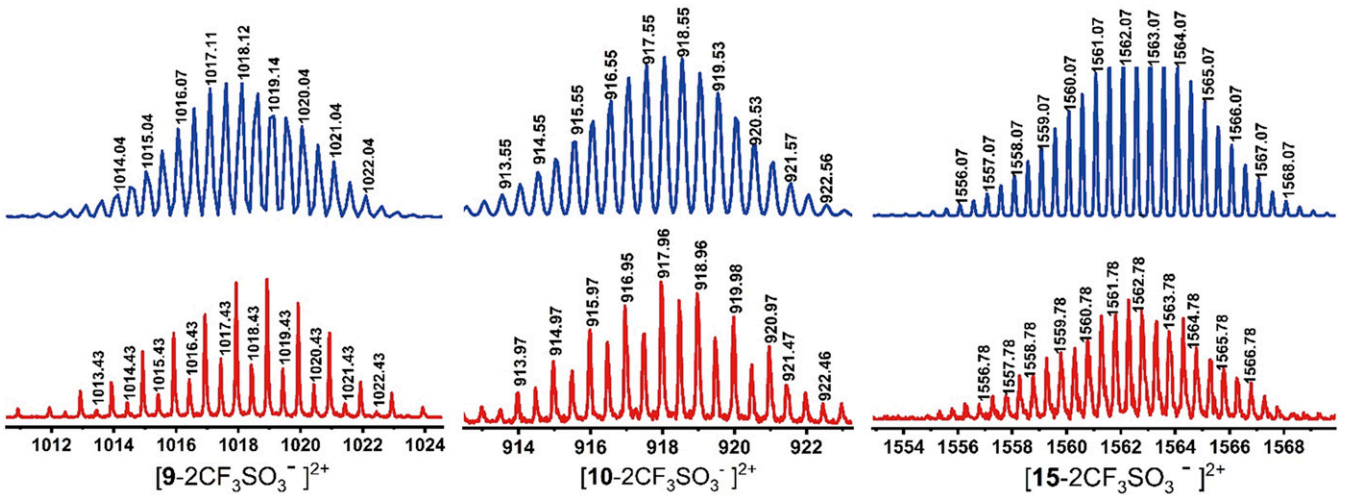

Fig. 6. Theoretically calculated (blue) and experimentally observed (red) ESI-MS isotopic patterns of $[9\text{-}2CF_3SO_3^-]^{2+}$ (*Left*), $[10\text{-}2CF_3SO_3^-]^{2+}$ (*Middle*), and $[15\text{-}2CF_3SO_3^-]^{2+}$ (*Right*) fragments.

cell-uptake by formation of the more-soluble larger assemblies with metal clip **6**. In addition, it is found that the IC_{50} values of complexes **9** and **15** toward A549 could dramatically decrease to about 10 times when exposure time was prolonged from 24 to 48 h (Table 1), indicating enhanced activity.

The cancer cell selectivity of the highly active compounds **9**, **12**, and **15** on the cytotoxities of cancer and normal cells were also investigated in human lung cancer cell A549, liver cancer cell HepG-2, normal human bronchial epithelioid cell (HBE), and liver epithelial cell (THLE-2) as summarized in Table 2. The

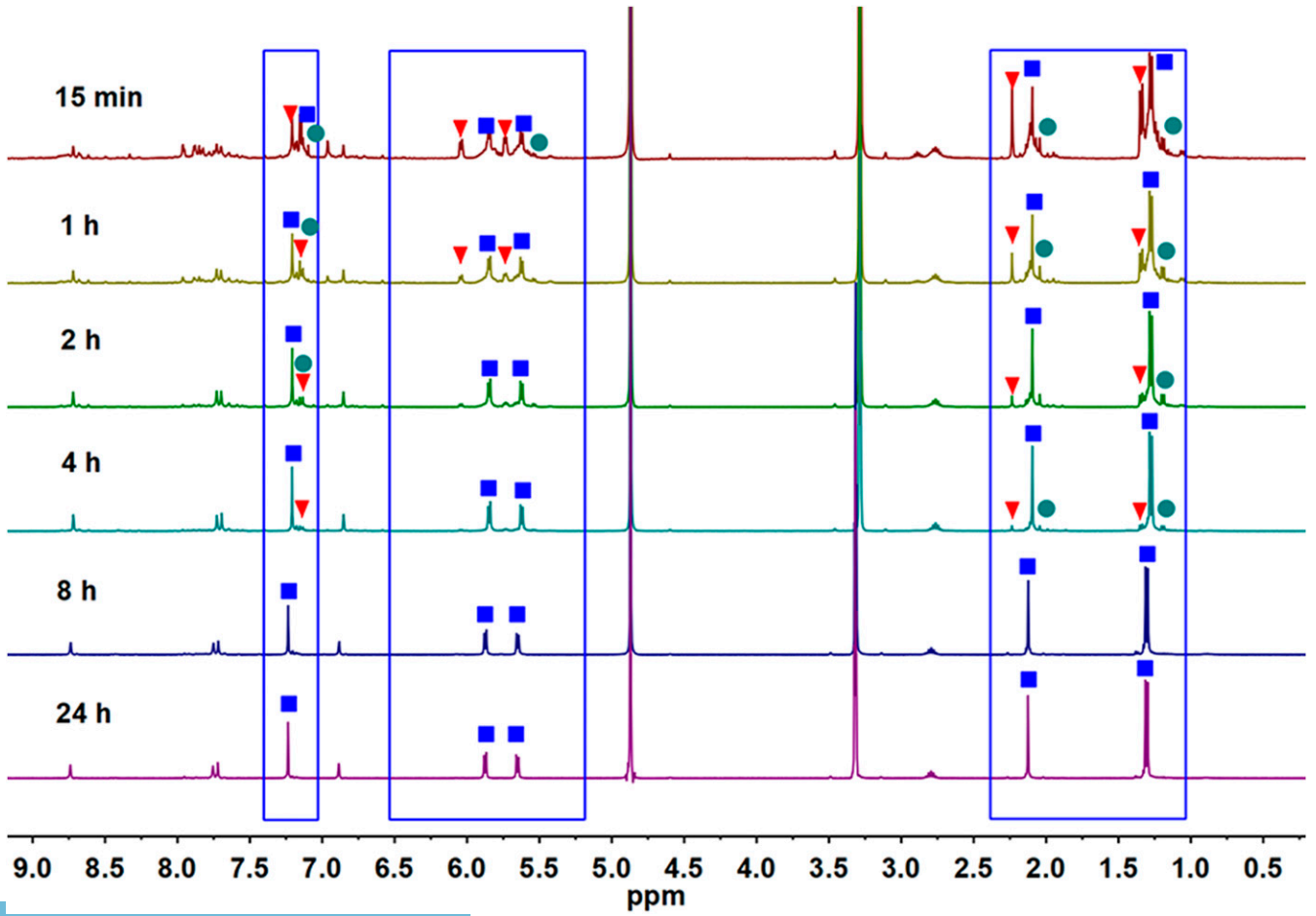

Fig. 7. The ^1H NMR spectra for complex **15** in CD_3OD.

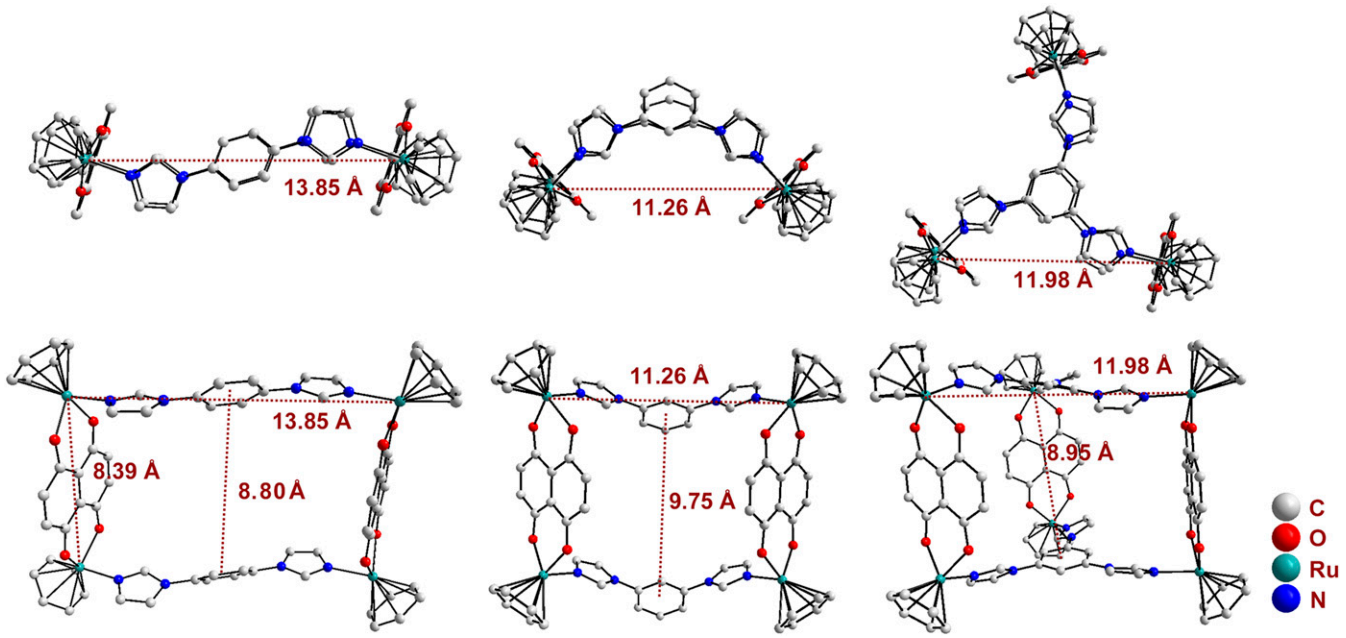

Fig. 8. A top and side view of the optimized structures of **9** (*Left*), **12** (*Middle*), and **15** (*Right*). The hydrogen atoms, methyl and isopropyl groups of *p*-cymene moiety have been omitted for clarity.

cytotoxities of the commonly used anticancer drugs, cisplatin, paclitaxel, and doxorubicin on these cells were also investigated for comparision (Table 2). Compounds **9** and **15** show decreased cytotoxicities in both of HBE and THLE-2 normal cells, whereas **12** shows low cytotocities in only THLE-2 normal cells. The selectivity index (SI), defined as the ratio of the IC_{50} value in THLE-2 to that in HepG-2, is 1.9 for **9**, 4.4 for **12**, 3.6 for **15**, and 2.1 for doxorubincin, but only 0.74 for paclitaxel and 0.27 for cisplatin. In general, compounds **9**, **12**, and **15** showed comparable cytotoxic potency to doxorubicin; however, they generally have lower IC_{50} values for cancer cells and higher SI values compared with cisplatin and paclitaxel, indicating that these self-assmebled large compounds are able to kill cancer cells more effectively and selectively than cisplatin and paclitaxel.

By comparing the activity and selectivity of **9**, **12**, and **15**, with the same Ru(II) building unit but different imidazole-based linkers, it is observed that the structure and geometry of these complexes due to the different imidazolyl ligand can have some effect on their anticancer activity and cancer cell selectivity. Among the three Ru complexes, complex **9** with the 180° ditopic **1**, having a rectangular geometry with dimension of 8.80 × 13.84 Å, exhibits good efficacy and selectivity toward most of tested cancer cells.

To probe whether the cytotoxicity and selectivity of complexes **9**, **12**, and **15** toward cancer cells might be caused by differences in cellular uptake efficiencies due to their different structure and geometry, A549 and HBE cells were treated with 10 μM of these complexes for 6 h, respectively, and the cellular levels of the ruthenium complexes were determined by inductivey coupled plasma-mass spectrometry (ICP-MS; Fig. 9). In A549 cells, the cellular uptake of Ru complexes is 2.99×10^{-2} pmol/10^6 cells for **9**, 0.96×10^{-2} pmol/10^6 cells for **12**, and 2.30×10^{-2} pmol/10^6 cells for **15**. These data show that the accumulation level of

Table 1. Cytotoxicities of Ru-based assemblies 1–15, cisplatin, and doxorubicin in human cancer cells over 48 h

	IC_{50} (μM)				
Complex	HCT-116	MDA-MB-231	MCF-7	HeLa	A549*
1	>50	>50	>50	>50	>50
2	>50	>50	>50	>50	>50
3	>50	>50	>50	>50	>50
4	>50	>50	>50	>50	>50
5	>50	>50	>50	>50	>50
6	6.12	5.54	8.25	37.00	22.62
7	>50	35.59	>50	>50	>50 (>50)
8	>50	>50	>50	>50	>50 (42.73)
9	0.37	1.83	1.39	2.18	1.14 (14.20)
10	>50	35.59	>50	>50	>50 (>50)
11	>50	>50	>50	>50	>50 (>50)
12	0.66	3.88	1.49	1.70	3.83 (7.57)
13	>50	>50	>50	>50	36.36 (>50)
14	>50	>50	>50	>50	31.83 (>50)
15	0.54	4.88	1.36	1.36	2.73 (20.37)
Cisplatin	21.32	>50	>50	35.12	27.59
Doxorubicin	9.60	0.27	0.29	1.28	4.35

*The data given brackets are IC_{50} for 24 h.

Table 2. Half-maximum inhibitory concentration (IC_{50}) values of metal complexes 9, 12, and 15 in A549 (lung cancer), HBE (bronchial epithelioid cells), HepG-2 (liver cancer), and THLE-2 (liver epithelial cells) for 48 h

	IC_{50} (μM)					
Complex	A549	HBE	SI*	HepG-2	THLE-2	SI†
9	1.14	4.31	3.8	1.74	3.27	1.9
12	3.83	3.39	0.89	0.78	3.40	4.4
15	2.73	3.95	1.4	1.20	4.30	3.6
Cisplatin	27.59	26.43	1.0	67.07	18.29	0.27
Doxorubicin	4.35	5.94	1.4	4.08	8.67	2.1
Paclitaxel	11.42	4.44	0.39	5.71	4.20	0.74

*SI is defined as IC_{50} in HBE/IC_{50} in A549.
†SI is defined as IC_{50} in THLE-2/IC_{50} in HepG-2.

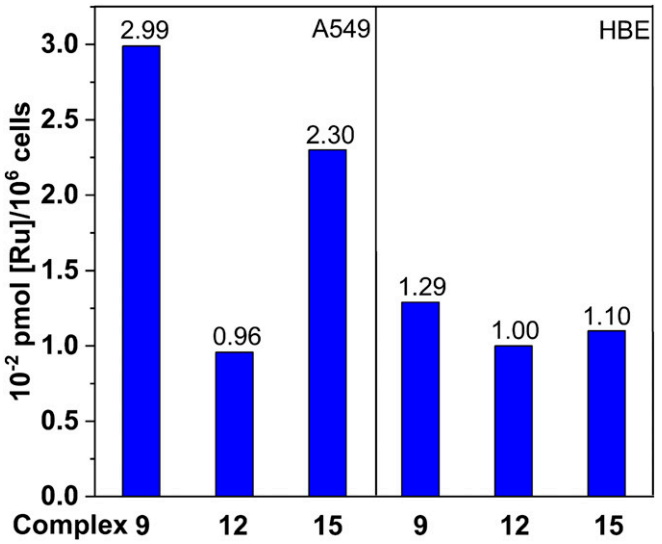

Fig. 9. Cellular accumulations of complexes **9**, **12**, and **15** in A549 and HBE cells.

compound **9** is the highest among the three complexes, which is consistent with its lowest IC_{50} value in A549 (1.14 μM). In addition, **9** and **15** exhibited stronger abilities to internalize into A549 cells than HBE cells, which is consistent with their good selectivity toward A549 over HBE cells. Hence, the cellular uptake efficiencies of these complexes in cancer cells relative to normal cells might contribute to their anticancer efficacy and selectivity.

It is known that DNA may be a potential target for ruthenium-based anticancer drugs, and many ruthenium compounds are known to have high selectivity for binding to DNA (58–62). An understanding of how these ruthenium assemblies interact with DNA is important for exploring the possible anticancer mechanism and helping to develop the most potent ruthenium based complex for selective and effective therapy. The potential binding ability of complexes **9**, **12**, and **15** with double-stranded ctDNA was investigated by UV-vis spectroscopy via titration of ctDNA into the solution of the Ru complex. The results, as seen in Fig. 10, show that the absorption peak at 452 nm for **9**, 473 nm for **12**, and 452 nm for **15** displayed a hyperchromic effect upon addition of ctDNA with bathochromic shift of the maximum wavelength (5 nm for **9**, 18 nm for **12**, and 5 nm for **15**). These results suggest that the complexes likely interact with ctDNA by an electrostatic binding mode, which is often caused by the interaction between positively charged drug molecules and negatively charged phosphoric moiety in DNA (63, 64). The magnitude of the binding constants (K_b) were calculated to be 5.6×10^4 M^{-1} for **9**, 1.6×10^4 M^{-1} for **12**, and 4.1×10^3 M^{-1} for **15**. Compound **9** with the 180° linear connector ligand **1** has the highest K_b in the complexes with ctDNA. Since these three complexes have the same Ru motif and a similar composition of the imidazole-based ligands, the difference between the binding constants is likely due to the different conformation of the imidazole-based ligands.

Conclusion

In summary, we report the synthesis of a series of arene-ruthenium (II) rectangles and trigonal prisms by the self-assembly of bidentate or tridentate imidazole-based ligands with *p*-cymene ruthenium (II) acceptors. Only the symmetrical isomers were selectively formed among several possible confomational isomers. The cytotoxicity of these complexes against HCT-116, MCF-7, HeLa, MDA-MB-23, A549, and HepG-2 cancer cell lines were evaluated, and rectangles **9** and **12** and prism **15** having donq-based scaffolds exhibit low IC_{50} values (hence, high activity) toward all tested cancer cell, and all are better than cisplatin. The complexes **9**, **12**, and **15** have good selectivity for HepG-2 caner cells compared with THLE-2 normal cells, while **9** and **15** have better selectivity for A549 than HBE cells. The UV-vis spectroscopy of the soultions of **9**, **12**, and **15** displayed a hyperchromic effect upon addition of ctDNA, and the data indicate that complex **9** with a 180° linear ligand **1** has the highest bonding constant (K_b) of 5.6×10^4 M^{-1} toward ctDNA.

Materials and Methods

The 1,4-bis(imidazol-1-yl)benzene (**1**) (65), 1,3-bis(imidazol-1-yl)benzene (**2**) (66), and 1,3,5-tri(1*H*-imidazol-1-yl)benzene (**3**) (67) were synthesized by the following previously reported methods. The acceptor $[Ru_2(\mu\text{-}\eta^4\text{-}OO\cap OO)(\eta^6\text{-}p\text{-cymene})_2](O_3SCF_3)_2$ (**4**–**6**) were synthesized under an atmosphere of dry nitrogen following the previously described procedures (68–70) (OO∩OO = oxalato, 2,5-dioxido-1,4-benzoquinonato and 5,8-dioxido-1,4-naphtoquinonato). All other chemicals were purchased from commercial sources and used as received. ^1H and ^{13}C NMR spectra were recorded on a Bruker AV400 spectrometer. Elemental analyses were performed with a Eurovector EuroEA3000 elemental analyzer. ESI-MS analyses were recorded on a Fisher LTQ-Orbitrap XL combined-type mass spectrometry. Absorption spectra of UV-vis were recorded on a TU-1901 UV-vis spectrophotometer at room temperature using 1-cm pathlength quartz cuvettes. The ruthenium content was determined by using an ICP-MS (Optima 7300 DV; Perkin-Elmer Company). The details of the synthesis, characterization, and biological experiments are given in *SI Appendix*.

ACKNOWLEDGMENTS. Y.S. thanks the National Natural Science Foundation of China (Grant 21571087), Major Projects of Natural Science Research in Jiangsu Province (Grant 15KJA150004), and TAPP of Jiangsu Higher Education Institutions for financial support. P.J.S. thanks the NIH (Grant R01-CA215157) for financial support.

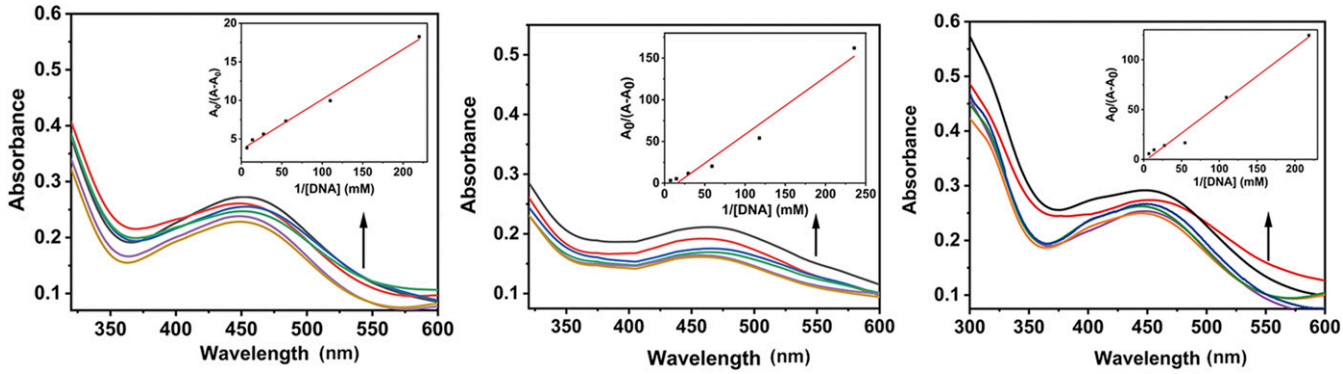

Fig. 10. UV-vis spectra of complexes **9** (*Left*), **12** (*Middle*), and **15** (*Right*) upon addition of ctDNA (0–0.1 M) in 5 mM Tris·HCl buffer solution (pH = 7.2). The arrows show the direction of change in absorbance upon increasing the concentration of ctDNA. (*Inset*) Plot of $A/(A - A_0)$ vs. 1/[DNA].

1. Jamieson ER, Lippard SJ (1999) Structure, recognition, and processing of cisplatin-DNA adducts. *Chem Rev* 99:2467–2498.
2. Long DF, Repta AJ (1981) Cisplatin: Chemistry, distribution and biotransformation. *Biopharm Drug Dispos* 2:1–16.
3. Rosenberg B, Van Camp L, Grimley EB, Thomson AJ (1967) The inhibition of growth or cell division in Escherichia coli by different ionic species of platinum(IV) complexes. *J Biol Chem* 242:1347–1352.
4. Wong E, Giandomenico CM (1999) Current status of platinum-based antitumor drugs. *Chem Rev* 99:2451–2466.
5. Siddik ZH (2003) Cisplatin: Mode of cytotoxic action and molecular basis of resistance. *Oncogene* 22:7265–7279.
6. Lazarević T, Rilak A, Bugarčić ZD (2017) Platinum, palladium, gold and ruthenium complexes as anticancer agents: Current clinical uses, cytotoxicity studies and future perspectives. *Eur J Med Chem* 142:8–31.
7. Zeng L, et al. (2017) The development of anticancer ruthenium(ii) complexes: From single molecule compounds to nanomaterials. *Chem Soc Rev* 46:5771–5804.
8. Blunden BM, Stenzel MH (2015) Incorporating ruthenium into advanced drug delivery carriers-an innovative generation of chemotherapeutics. *J Chem Technol Biotechnol* 90:1177–1195.
9. Agonigi G, et al. (2015) Synthesis and antiproliferative activity of new ruthenium complexes with ethacrynic-acid-modified pyridine and triphenylphosphine ligands. *Inorg Chem* 54:6504–6512.
10. Wang T, et al. (2016) A ferrocenyl pyridine-based Ru(II) arene complex capable of generating center dot OH and O-1(2) along with photoinduced ligand dissociation. *RSC Adv* 6:45652–45659.
11. Murray BS, Babak MV, Hartinger CG, Dyson PJ (2016) The development of RAPTA compounds for the treatment of tumors. *Coord Chem Rev* 306:86–114.
12. Dougan SJ, Sadler PJ (2007) The design of organometallic ruthenium arene anticancer agents. *Chimia* 61:704–715.
13. Morris RE, et al. (2001) Inhibition of cancer cell growth by ruthenium(II) arene complexes. *J Med Chem* 44:3616–3621.
14. Betanzos-Lara S, Salassa L, Habtemariam A, Sadler PJ (2009) Photocontrolled nucleobase binding to an organometallic Ru(II) arene complex. *Chem Commun (Camb)* 43:6622–6624.
15. Grozav A, et al. (2015) Synthesis, anticancer activity, and genome profiling of thiazolo arene ruthenium complexes. *J Med Chem* 58:8475–8490.
16. Li J, et al. (2018) Half-sandwich iridium(III) and ruthenium(II) complexes containing P^P-chelating ligands: A new class of potent anticancer agents with unusual redox features. *Inorg Chem* 57:1705–1716.
17. Ma L, et al. (2018) A cancer cell-selective and low-toxic bifunctional heterodinuclear Pt(IV)-Ru(II) anticancer prodrug. *Inorg Chem* 57:2917–2924.
18. Katarzyna M, Anna S, Zielinska-Blizniewska H, Ireneusz M (2018) An evaluation of the antioxidant and anticancer properties of complex compounds of copper (II), platinum (II), palladium (II) and ruthenium (III) for use in cancer therapy. *Mini Rev Med Chem* 18:1373–1381.
19. Chyba J, Novák M, Munzarová P, Novotný J, Marek R (2018) Through-space paramagnetic NMR effects in host-guest complexes: Potential ruthenium(III) metallodrugs with macrocyclic carriers. *Inorg Chem* 57:8735–8747.
20. Sahyon HA, El-Bindary AA, Shoair AF, Abdellatif AA (2018) Synthesis and characterization of ruthenium(III) complex containing 2-aminomethyl benzimidazole, and its anticancer activity of in vitro and in vivo models. *J Mol Liq* 255:122–134.
21. Rademaker-Lakhai JM, van den Bongard D, Pluim D, Beijnen JH, Schellens JHM (2004) A Phase I and pharmacological study with imidazolium-trans-DMSO-imidazole-tetrachlororuthenate, a novel ruthenium anticancer agent. *Clin Cancer Res* 10:3717–3727.
22. Hartinger CG, et al. (2006) From bench to bedside–Preclinical and early clinical development of the anticancer agent indazolium trans-[tetrachlorobis(1H-indazole)ruthenate(III)] (KP1019 or FFC14A). *J Inorg Biochem* 100:891–904.
23. Hartinger CG, et al. (2008) KP1019, a new redox-active anticancer agent–Preclinical development and results of a clinical phase I study in tumor patients. *Chem Biodivers* 5:2140–2155.
24. Bytzek AK, Koellensperger G, Keppler BK, G Hartinger C (2016) Biodistribution of the novel anticancer drug sodium trans-[tetrachloridobis(1*H*-indazole)ruthenate(III)] KP-1339/IT139 in nude BALB/c mice and implications on its mode of action. *J Inorg Biochem* 160:250–255.
25. Fujita M, Tominaga M, Hori A, Therrien B (2005) Coordination assemblies from a Pd(II)-cornered square complex. *Acc Chem Res* 38:369–378.
26. Chakrabarty R, Mukherjee PS, Stang PJ (2011) Supramolecular coordination: Self-assembly of finite two- and three-dimensional ensembles. *Chem Rev* 111:6810–6918.
27. Cook TR, Stang PJ (2015) Recent developments in the preparation and chemistry of metallacycles and metallacages via coordination. *Chem Rev* 115:7001–7045.
28. Xu L, Wang YX, Chen LJ, Yang HB (2015) Construction of multiferrocenyl metallacycles and metallacages via coordination-driven self-assembly: From structure to functions. *Chem Soc Rev* 44:2148–2167.
29. Barry NPE, Govindaswarny P, Furrer J, Suss-Fink G, Therrien B (2008) Organometallic boxes built from 5,10,15,20-tetra(4-pyridyl)porphyrin panels and hydroxyquinonato-bridged diruthenium clips. *Inorg Chem Commun* 11:1300–1303.
30. Schmitt F, et al. (2008) Ruthenium porphyrin compounds for photodynamic therapy of cancer. *J Med Chem* 51:1811–1816.
31. Vajpayee V, et al. (2011) Self-assembly of cationic, hetero- or homo-nuclear Ru(II) macrocyclic rectangles and their photophysical, electrochemical and biological studies. *Organometallics* 30:6482–6489.
32. Vajpayee V, et al. (2011) Self-assembled arene-ruthenium-based rectangles for the selective sensing of multi-carboxylate anions. *Chemistry* 17:7837–7844.
33. Dubey A, et al. (2013) Anticancer potency and multidrug-resistant studies of self-assembled arene-ruthenium metallarectangles. *Chemistry* 19:11622–11628.
34. Mishra A, Kang SC, Chi KW (2013) Coordination-driven self-assembly of arene-ruthenium compounds. *Eur J Inorg Chem* 2013:5222–5232.
35. Pal M, Nandi U, Mukherjee D (2018) Detailed account on activation mechanisms of ruthenium coordination complexes and their role as antineoplastic agents. *Eur J Med Chem* 150:419–445.
36. Mari C, Pierroz V, Ferrari S, Gasser G (2015) Combination of Ru(ii) complexes and light: New frontiers in cancer therapy. *Chem Sci (Camb)* 6:2660–2686.
37. Nazarov AA, Hartinger CG, Dyson PJ (2014) Opening the lid on piano-stool complexes: An account of ruthenium(II)-arene complexes with medicinal applications. *J Organomet Chem* 751:251–260.
38. Wang K, Gao E (2014) Recent advances in multinuclear complexes as potential anticancer and DNA binding agents. *Anticancer Agents Med Chem* 14:147–169.
39. Mannancherril V, Therrien B (2018) Strategies toward the enhanced permeability and retention effect by increasing the molecular weight of arene ruthenium metallaassemblies. *Inorg Chem* 57:3626–3633.
40. Singh AK, Pandey DS, Xu Q, Braunstein P (2014) Recent advances in supramolecular and biological aspects of arene ruthenium(II) complexes. *Coord Chem Rev* 270: 31–56.
41. Mattsson J, et al. (2010) Drug delivery of lipophilic pyrenyl derivatives by encapsulation in a water soluble metalla-cage. *Dalton Trans* 39:8248–8255.
42. Matsumura Y, Maeda H (1986) A new concept for macromolecular therapeutics in cancer chemotherapy: Mechanism of tumoritropic accumulation of proteins and the antitumor agent smancs. *Cancer Res* 46:6387–6392.
43. Shanmugaraju S, Bar AK, Mukherjee PS (2010) Ruthenium-oxygen coordination-driven self-assembly of a $Ru(II)_8$ incomplete prism: Synthesis, structure, and shape-selective molecular recognition study. *Inorg Chem* 49:10235–10237.
44. Mirtschin S, Slabon-Turski A, Scopelliti R, Velders AH, Severin K (2010) A coordination cage with an adaptable cavity size. *J Am Chem Soc* 132:14004–14005.
45. Yao LY, Qin L, Xie TZ, Li YZ, Yu SY (2011) Synthesis and anion sensing of water-soluble metallomacrocycles. *Inorg Chem* 50:6055–6062.
46. Saha R, Ghosh AK, Samajdar RN, Mukherjee PS (2018) Self-assembled Pd^{II}_6 molecular spheroids and their proton conduction property. *Inorg Chem* 57:6540–6548.
47. Scherr N, Röltgen K, Witschel M, Pluschke G (2012) Screening of antifungal azole drugs and agrochemicals with an adapted alamarBlue-based assay demonstrates antibacterial activity of croconazole against Mycobacterium ulcerans. *Antimicrob Agents Chemother* 56:6410–6413.
48. Wang B, Côté AP, Furukawa H, O'Keeffe M, Yaghi OM (2008) Colossal cages in zeolitic imidazolate frameworks as selective carbon dioxide reservoirs. *Nature* 453:207–211.
49. Cai SL, et al. (2017) Temperature/anion-dependent self-assembly of Co(II) coordination polymers based on a heterotopic imidazole-tetrazole-bifunctional ligand: Structures and magnetic properties. *Inorg Chem Commun* 84:10–14.
50. Schröder K, et al. (2009) Design of and mechanistic studies on a biomimetic iron-imidazole catalyst system for epoxidation of olefins with hydrogen peroxide. *Chemistry* 15:5471–5481.
51. Biswal D, et al. (2017) Syntheses, crystal structures, DFT calculations, protein interaction and anticancer activities of water soluble dipicolinic acid-imidazole based oxidovanadium(iv) complexes. *Dalton Trans* 46:16682–16702.
52. Bhandari K, Srinivas N, Shiva Keshava GB, Shukla PK (2009) Tetrahydronaphthyl azole oxime ethers: The conformationally rigid analogues of oxiconazole as antibacterials. *Eur J Med Chem* 44:437–447.
53. Emami S, et al. (2008) 2-Hydroxyphenacyl azoles and related azolium derivatives as antifungal agents. *Bioorg Med Chem Lett* 18:141–146.
54. Anderson EB, Long TE (2010) Imidazole- and imidazolium-containing polymers for biology and material science applications. *Polymer (Guildf)* 51:2447–2454.
55. Zhang L, Peng XM, Damu GLV, Geng RX, Zhou CH (2014) Comprehensive review in current developments of imidazole-based medicinal chemistry. *Med Res Rev* 34: 340–437.
56. Samanta D, Shanmugaraju S, Adeyemo AA, Mukherjee PS (2014) Self-assembly of discrete metallamacrocycles employing half-sandwich octahedral diruthenium(II) building units and imidazole-based ligands. *J Organomet Chem* 751:703–710.
57. Adeyemo AA, Shanmugaraju S, Samanta D, Mukherjee PS (2016) Template-free coordination-driven self-assembly of discrete hexanuclear prismatic cages employing half-sandwich octahedral Ru-2(II) acceptors and triimidazole donors. *Inorg Chim Acta* 440:62–68.
58. Zhao R, et al. (2009) Nuclear targets of photodynamic tridentate ruthenium complexes. *Dalton Trans,* 10926–10931.
59. Zeng L, Xiao Y, Liu J, Tan L (2012) Synthesis, characterization, DNA-binding and cytotoxic properties of Ru(II) complexes: $[Ru(MeIm)_4L]^{2+}$ (MeIm=1-methylimidazole, L=phen, ip and pip). *J Mol Struct* 1019:183–190.
60. Aird RE, et al. (2002) In vitro and in vivo activity and cross resistance profiles of novel ruthenium (II) organometallic arene complexes in human ovarian cancer. *Br J Cancer* 86:1652–1657.
61. Pascu GI, Hotze ACG, Sanchez-Cano C, Kariuki BM, Hannon MJ (2007) Dinuclear ruthenium(II) triple-stranded helicates: Luminescent supramolecular cylinders that bind and coil DNA and exhibit activity against cancer cell lines. *Angew Chem Int Ed Engl* 46: 4374–4378.
62. Wu K, et al. (2013) Competitive binding sites of a ruthenium arene anticancer complex on oligonucleotides studied by mass spectrometry: Ladder-sequencing versus top-down. *J Am Soc Mass Spectrom* 24:410–420.
63. Barone G, et al. (2013) DNA-binding of nickel(II), copper(II) and zinc(II) complexes: Structure–affinity relationships. *Coord Chem Rev* 257:2848–2862.
64. Kenney RM, Buxton KE, Glazier S (2016) Investigating the impacts of DNA binding mode and sequence on thermodynamic quantities and water exchange values for two small molecule drugs. *Biophys Chem* 216:9–18.

65. Li F, Hor TSA (2009) Facile synthesis of nitrogen tetradentate ligands and their applications in Cu(I)-catalyzed N-arylation and azide-alkyne cycloaddition. *Chemistry* 15: 10585–10592.
66. Charra V, de Fremont P, Breuil PAR, Olivier-Bourbigou H, Braunstein P (2015) Silver(I) and copper(I) complexes with bis-NHC ligands: Dinuclear complexes, cubanes and coordination polymers. *J Organomet Chem* 795:25–33.
67. Zhang S, Yang S, Lan J, Yang S, You J (2008) Helical nonracemic tubular coordination polymer gelators from simple achiral molecules. *Chem Commun (Camb)*, 6170–6172.
68. Yan H, Süss-Fink G, Neels A, Stoeckli-Evans H (1997) Mono-, di- and tetra-nuclear p-cymeneruthenium complexes containing oxalato ligands. *J Chem Soc Dalton Trans*, 4345–4350.
69. Therrien B, Süss-Fink G, Govindaswamy P, Renfrew AK, Dyson PJ (2008) The "complex-in-a-complex" cations [(acac)2M subset Ru6(p-iPrC6H4Me)6(tpt)2(dhbq)3]6+: A trojan horse for cancer cells. *Angew Chem Int Ed Engl* 47:3773–3776.
70. Barry NPE, Therrien B (2009) Host-guest chemistry in the hexanuclear (arene)ruthenium metalla-prismatic cage $[Ru_6(p\text{-cymene})_6(tpt)_2(dhnq)_3]^{6+}$. *Eur J Inorg Chem* 2009: 4695–4700.